This is the Pre-Published Version.

The following publication Lu, Y., Gao, X., Jiang, L., Chen, Z., Wang, T., Jie, J., ... & Li, T. (2017). Directly cast bulk eutectic and near-eutectic high entropy alloys with balanced strength and ductility in a wide temperature range. Acta materialia, 124, 143-150 is available at https://doi.org/10.1016/j.actamat.2016.11.016.

Directly cast eutectic and near-eutectic high entropy alloys with balanced strength and ductility at both room and cryogenic temperatures

Yiping Lu[1,2], Li Jiang[1], Zongning Chen[1],Yong Dong[1], Tongmin Wang[1,*], Huijun Kang[1], Jinchuan Jie[1], Zhiqiang Cao[1], Haihui Ruan[4], Sheng Guo[3,*], Tingju Li[1,*]

[1] Key Laboratory of Solidification Control and Digital Preparation Technology (Liaoning Province), School of Materials Science and Engineering, Dalian University of Technology, Dalian 116024, P.R. China

[2] State Key Laboratory of Metastable Materials Science and Technology, Yanshan University, Qinhuangdao, 066004, P. R. China

[3] Surface and Microstructure Engineering Group, Materials and Manufacturing Technology, Chalmers University of Technology, SE-41296, Gothenburg, Sweden

[4] Department of Mechanical Engineering, The Hong Kong Polytechnic University, Hung Hom, Hong Kong, P. R. China

* Author to whom correspondence should be addressed.

E-mail: tmwang@dlut.edu.cn; sheng.guo@chalmers.se; tjuli@dlut.edu.cn

Tel.: +86 411 84709400; Fax: +86 411 84708940

Abstract

High entropy alloys usually possess weak liquidity and castability, and considerable compositional inhomogeneity, mainly because they contain multiple elements with high concentrations. As a result, large-scale production of high entropy alloys by casting is limited. To address the issue, the concept of eutectic high entropy alloys was proposed, which has led to some promise in achieving good quality industrial scale high entropy alloy ingots, and more importantly also good mechanical properties. In the practical large-scale casting, the actual composition of designed eutectic high entropy alloy could potentially deviate from the eutectic composition. The influence of such deviation on mechanical properties of eutectic high entropy alloys is important for industrial production, which constitutes the topic of the current work. Here we prepared industrial-scale high entropy alloy ingots near the eutectic composition: hypoeutectic alloy, eutectic alloy and hypereutectic alloy. Our results showed that the deviation from eutectic composition does not significantly affect the mechanical properties, castability and the good mechanical properties of eutectic high entropy alloys can be achieved in a wide compositional range, and at both room and cryogenic temperatures. Our results suggested that eutectic high entropy alloys with simultaneous high strength and high ductility, and good liquidity and castability can be readily adapted to large-scale industrial production. The deformation behavior and microstructure evolution of the eutectic and near-eutectic HEAs were thoroughly studied using a combination of techniques, including strain measurement by digital image correlation, in-situ synchrotron X-ray diffraction, and transmission electron microscopy.

Keywords: High entropy alloys; Eutectic alloys; Mechanical properties; In-situ X-ray diffraction; Digital image correlation; Industrial scale casting

© 2016. This manuscript version is made available under the CC-BY-NC-ND 4.0 license http://creativecommons.org/licenses/by-nc-nd/4.0/

1. Introduction

Recently, a new type of alloys, high entropy alloys (HEAs) or multi-principal-element alloys, is becoming new research frontier in the metallic materials community [1-14]. Compared to conventional metallic alloys based on one or two principal elements, HEAs generally contain at least four principal elements. The concept of HEAs is a breakthrough to the alloy design in traditional physical metallurgy, and opens a new field for explorations of new materials and new properties [13, 15]. Although the high configuration entropy in HEAs helps to stabilize solid solutions (against compound phases), previous studies have showed that most HEAs contain multiple phases rather than a single-phase solid solution [2, 16-18]. From the alloy preparation perspective, most HEAs are made by casting, although the powder metallurgy route is also gaining more attention [19, 20]. Casting of HEAs, particularly at a large scale (kilogram scale) is quite often a challenge, as most HEAs possess weak liquidity and castability (see Fig. S1 in the Supplementary Information for a demonstration) and considerable chemical inhomogeneity [21], which retards their industrial application. From the mechanical properties perspective, it is already known that in general single-phased body-centered cubic (bcc)-structured HEAs have limited ductility [22], while single-phased face-centered cubic (fcc)-structured HEAs could have high ductility but their strength is low [23]. How to reach the both high strength and high ductility is another challenge for the engineering application of HEAs.

To address the above mentioned problems facing the real application of HEAs, the current authors proposed to use the eutectic alloy concept to design HEAs, aiming at good castability of eutectic alloys and composite structure to resolve the strength-ductility trade-off [21, 24]. Our initial efforts in making eutectic HEAs (EHEAs) have led to kilogram-scale $AlCoCrFeNi_{2.1}$ HEA with good liquidity and castability, which also exhibits good mechanical properties at both room temperature and elevated temperatures up to 700 °C [21].

Practically, the actual composition of EHEAs could deviate from the designed eutectic composition, especially for the large-scale casting. How would the deviation from the eutectic composition affect mechanical properties of EHEAs? The acceptable compositional range for desired mechanical properties is certainly important for the industrial production of EHEAs, but remains unexplored. This motivates the current work. Here we prepared industrial-scale ingots near the previously studied eutectic composition, $AlCoCrFeNi_{2.1}$, and tested how the mechanical properties of EHEAs vary in a compositional range near the eutectic composition. We chose to use directly cast materials for the study, since we are expecting to avoid subsequent thermomechanical treatments by developing sufficiently good as-cast materials. Certainly, the performance of as-cast materials that are reported here can be further improved by thermomechanical treatments [21, 24].

2. Experimental

The master alloy of hypoeutectic $AlCoCrFeNi_{2.0}$ (Ni2.0), eutectic $AlCoCrFeNi_{2.1}$ (Ni2.1), and hypereutectic $AlCoCrFeNi_{2.2}$ (Ni2.2) were prepared from commercially pure elements (Al, Co, Ni: 99.9 wt. %; Cr, Fe: 99.5~99.6 wt.%). The raw elements were alloyed in a BN crucible in the vacuum induction melting furnace. The BN crucible was heated to 600 °C and held for 1 hour to remove the water vapor, before putting into the furnace. The pouring temperature was set to be 1500 ^{o}C. An IRTM-2CK infrared pyrometer was employed to monitor the temperature with an absolute accuracy of ± 2 ^{o}C. Approximately 2.5 kg of master alloys were melted, superheated and poured into a MgO crucible with the length of 220 mm, upper inner diameter of 62 mm and bottom inner diameter of 50 mm. In all cases, the furnace chamber was first evacuated to 6×10^{-2} Pa and then backfilled with high-purity argon gas to reach 0.06 MPa. The microstructure and composition of the alloy were investigated by scanning electron microscope (SEM, Zeiss Supra 55) equipped with an attached X-ray energy dispersive spectrometer (EDS). The phase constitution of the alloy was characterized by the X-ray diffractometer (XRD, Shimadzu XRD-6000) using a Cu target, with the scanning rate of 4°/min and the 2θ scanning range of 20°-100°. Room-temperature (RT) tensile tests were performed using the Instron 5569 testing machine at a constant strain rate of 1×10^{-3} s^{-1}, and the bar-shaped tensile test samples had a gauge length of 20 mm, width of 3 mm and thickness of 3 mm. Cryogenic tensile tests at -70 ^{o}C and -196 ^{o}C were performed on rod-shaped samples with a gauge length of 28 mm and diameter of 5 mm, using a MTS 810 testing machine at an strain rate of 1×10^{-3} s^{-1}. Before tensile tests, the specimens and grips were immersed in a liquid nitrogen bath for about 5-10 min; during tensile tests, the specimens stayed completely submerged in the liquid nitrogen and the temperature was measured by the thermocouple. After stretching to tensile rupture, thin sheets with a thickness of 300 μm were cut from the cross section of the gauge areas for microstructure observation using transmission electron microscopy (TEM, JEM-2100F). TEM samples were first mechanically ground to 45 μm in thickness, then punched into foils with a diameter of 3 mm, and finally thinned by a twin-jet electropolisher using the electrolyte made of 90 vol. % alcohol and 10 vol. % perchloric acid at a voltage of 20 kV. To further understand the deformation behavior, the strain field of the $AlCoCrFeNi_{2.1}$ EHEA sheet within the gauge length was further mapped by the Nakazima test (strain measurement by digital image correlation, SMDIC, see Fig. S2). Tensile tests were carried out on a Series LFM-20 kN electromechanical universal testing machine with a strain rate of 1×10^{-3} s^{-1} at room temperature. Bar-shaped tensile samples with a gauge length of 20 mm, width of 3 mm and thickness of ~ 2 mm were grounded and polished before tension. The measurement to evaluate the strain needs an initial high-contrast stochastic pattern of spots on the outer surface of the test sample, which was achieved by first spraying a background of adhesive and flexible matte white paint on the tensile samples, and then spraying a fine layer of spots of black paint onto the background. From the beginning of loading to the final failure, the evolution of the black spots was recorded using two CCD cameras positioned in a non-symmetrical configuration: first one directly in front of the specimen and the second one at about 32 degrees to the normal direction of the specimen. This setting allows performing 3D DIC analysis. The CCD camera recorded 2 images per second during the tension test, which were processed using the ARAMIS software to determine the full-field displacements. For understanding the phase transformation during the tensile testing, in-situ synchrotron XRD analysis was carried out on the 4W1A beamline at Beijing Synchrotron Radiation Facility (BSRF), China. The synchrotron X-ray with the wavelength of 1.54 Å was irradiated on the tensile test sheets from the beginning of loading to final fracture. Dogbone-shaped specimens with a gauge length of 13 mm and cross-section of 3 mm ×1 mm were uniaxially tensile tested using a specially designed testing device (see Fig. S3) at a stretching speed of 10 μm s^{-1}. Before testing, the specimens were grinded, polished and cleaned with alcohol. The tensile specimen was positioned at 45° from the incident beam, while a fan-shaped detector with the apex angle of 120° was set at the direction of the emergent beam (Fig. S4). The incident beam and the detector were kept within the same plane. The scanning range was set from 20° to 160°, as main peaks are concentrated in this range. The diffraction patterns were collected every per 30 seconds. Then diffraction angle 2θ corresponding to the (hkl) crystal plane was converted to the lattice spacing, *d*, using the Bragg's law. The lattice strain perpendicular to the (hkl) crystal plane was determined from the shifts of the lattice spacing. Specifically, the lattice strains ε_{hkl} during an applied load can be calculated from the equation $\varepsilon_{hkl} = (d_{hkl}-d_{hkl,0})/d_{hkl,0}$, in which d_{hkl} is determined from the hkl reflection during tension, and $d_{hkl,0}$ refers to the value for zero load. Finally, lattice strain as a function of loading time for five families of (hkl) crystal planes were obtained during the tensile loading at RT.

3. Results and discussion

3.1 Microstructure and phase identification

Industrial scale $AlCoCrFeNi_x$ (x=2.0, 2.1 and 2.2) ingots of ~ 2.5 kg each in weight were prepared. All the ingots exhibited an excellent castability during the casting process, similar to most conventional eutectic alloys. SEM images of the cast microstructure of Ni2.0, Ni2.1 and Ni2.2 ingots are shown in Fig.1 (a-c). Even at such a large ingot, the dominating microstructure in hypoeutectic (Ni2.0) and hypereutectic (Ni2.2) HEAs are fairly uniform and fine lamella, very similar to those in the EHEA (Ni2.1), except for the existence of some small amounts of primary phases. Inter-lamellar spacing in all three HEAs ingots are about 1~3 μm. According to the microstructure and EDS analysis, the hypoeutectic Ni2.0 alloy comprises a small amount of primary NiAl-rich phase plus eutectic FeCr-rich phase/NiAl-rich phase, while the hypereutectic Ni2.2 alloy comprise a small amount of primary FeCr-rich phase plus eutectic FeCr-rich phase/NiAl-rich phase. The FeCr-rich phase and NiAl-rich phase have been previously identified to be fcc and B2 phase, respectively [21]. The XRD patterns shown in Fig. 2 further confirm that only a mixture of fcc and B2 phases are observed in Ni2.0, Ni2.1 and Ni2.2 HEAs, and the amount of fcc phase increases when the alloy compositions shifts from hypoeutectic to hypereutectic composition, in agreement with the microstructural observation. TEM observations (see section 3.5 and Ref. [24]) further show that the fcc phase is actually ordered, with the $L1_2$ structure.

3.2 Tensile properties

The hypoeutectic Ni2.0 and hypereutectic Ni2.2 alloys exhibit a combination of both high strength and high ductility, close to that of the Ni2.1 EHEA. Specifically, from the RT engineering stress-strain curves given in Fig. 3, the yield and fracture stresses of Ni2.0, Ni2.1 and Ni2.2 alloys are almost the same, which are ~ 545 MPa and ~1100 MPa, respectively. Ni2.0 and Ni2.1 alloys fracture at 16-17% elongation, while that of the hypereutectic Ni2.2 alloy reaches ~20%, owing to the highest content of the soft fcc phase among three alloys.

The engineering stress-stain curves for Ni2.0, Ni2.1 and Ni2.2 alloys at cryogenic temperatures are shown in Figs. 4 and 5. At -70 ºC, the yield stress, fracture stress and elongation of Ni2.0, Ni2.1 and Ni2.2 alloys are 580 MPa/1034 MPa/10.5%, 595 MPa/1168

MPa/15.8%, 570 MPa/1143 MPa/18.0%, respectively. Compared to the RT properties, both the yield strength and fracture strength increase slightly, which is in trade-off of elongation. Still, a quite good combination of strength and ductility is maintained at -70 ºC, from hypoeutectic to eutectic to hypereutectic alloys. At even lower temperature of -196 ºC, the yield strength continues to increase, to ~ 700 MPa for all three alloys, while the ductility decreases sharply, to 4% for hypoeutectic Ni2.0 alloy which contains more hard/brittle B2 phase, and to 7% and 9% for eutectic and hypereutectic alloys. The early fracture also limits the fracture strength of three alloys to 1000-1100 MPa. With decreasing temperature, dislocation motions become more difficult due to the reduced thermal energy for crossing Peierls-Nabarro barriers, and more dislocations accumulate inside the crystal before moving out to accommodate the plastic strain, thus leading to less ductility. This scenario is more severe in the bcc phase than in the fcc phase due to the much higher temperature sensitivity of the *Peierls-Nabarro force* in the former [23, 25], which explains why the hypoeutectic Ni2.0 alloy containing more of bcc phase shows the lowest ductility at -196 ºC, while the hypereutectic Ni2.2 alloy containing more fcc phase can keep a decent ductility (of ~ 9% elongation) at the same temperature.

Fig. 6 shows the fracture surface morphology of the as-cast Ni2.1 EHEA at cryogenic temperatures and at room temperature. Ni2.0 and Ni2.2 alloys present similar fracture morphology, so only the Ni2.1 alloy is chosen for analysis here. For the same reason, only results from the Ni2.1 alloy are given in the following discussions to represent all three alloys unless otherwise stated. As shown in Fig. 6, the fracture surface features mainly trench-like microstructures. By connecting the fcc/B2 composite structure in the Ni2.1

EHEA, it is reasonable to infer the formation mechanism of these trench-like microstructures: during the tensile deformation, the hard B2 phase is barely deformed while the soft fcc phase is stretched; the fcc phase then gradually becomes thinner and edges up, leaving the barely deformed bcc phase at the bottom of the trench. This assumption is supported by the EDS analysis made at the fractured surface. The fact that there exist more trench-like microstructures in the -196 ^{o}C fractured alloy also lends support to the above given argument on the temperature-sensitive flow stress of the bcc phase.

3.3 The Nakazima test

It is of interest to note that although presenting a large ductility, necking is not obvious in tensile tests at both RT and cryogenic temperatures (see Fig. 7). The mechanism for this peculiar deformation deserves further studies. The Nakazima tests (SMDIC) were therefore conducted to map the full-field strain distribution. Besides the eutectic and near-eutectic HEAs, the as-cast fcc-structured pure Ni and bcc-structured pure Fe specimens were also tested for comparison. Fig. 8(a) shows the strain field of the EHEA specimen within the gauge length at different stages during tension. In the early stages of deformation, the strain is distributed almost uniformly throughout the entire loading area. After a few seconds, strain localization occurs within a narrow band at some location. Subsequently, the other strain localization appears at a new location. During the course of deformation, it is found that the high-strain and the low-strain regions alternatively appear, exhibiting a wavy strain distribution. This feature is in line with the negligible necking observed in three types of HEAs, which however is markedly different from the conventional understanding of deformation behavior of strain-hardening materials. If the strain hardening rate is uniform, strain localization should occur in one narrow zone, which leads to necking and fracture. This is the case for pure Ni and Fe as shown in Fig. 8(b-c). For both pure Ni and pure Fe, the strain is first distributed almost uniformly within the gauge length at the early stages of loading. With further deformation, the strain starts to localize in just one narrow band (much faster in bcc-Fe compared to fcc-Ni), finally leading to the necking and fracture of the tensile sample. The distinct deformation behavior of EHEAs in comparison with pure metals may be understood based on the fine-lamella composite structure. During tensile deformation, the soft regions (the fcc phase in this case) will deform more, while the hard regions (B2 phase) will stay less deformed. With further deformation, the soft regions become sufficiently hardened such that the initially hard regions have to undergo some more deformation. Due to the fine lamellar structure in eutectic alloys and therefore the alternative arrangement of soft and hard regions, the wavy strain distribution shown in Fig. 8(a) is observed. It should be stressed that the "wave length" of the wavy strain field observed in Fig. 8(a) is much larger than the width of fcc and B2 lamella. Therefore, our understanding of deformation behavior of EHEA based on lamella microstructures is merely qualitative. The main point is that the actual hardening behavior in EHEA is not uniform, which leads to the non-uniform strain field during the whole course of plastic deformation till fracture. Clearly, the hard B2 phase renders the alloy with high strength, while the soft fcc phase enables the alloy to have some decent ductility. Such a combination brings about the good balance of high strength and high ductility in the EHEA. However, the very limited deformability of the hard B2 phase also restricts the further deformation of the alloy. When the flow stress of the fcc phase is raised to surpass the strength of the B2 phase, it soon comes to the point that the alloy will fracture by cracking initiating from pre-existing defected regions.

3.4 In-situ synchrotron X-ray diffraction test

The simultaneous achievement of high strength and high ductility in large-scale directly cast hypoeutectic, eutectic and hypereutectic HEAs is quite appealing, which is also seldom seen in both conventional alloys and other HEAs reported previously, at the as-cast state. It is intriguing to understand whether any phase transformation occurs during the deformation process. For this purpose, in-situ synchrotron XRD under uniaxial tensile loading at RT was conducted for the Ni2.1 EHEA. Fig. 9(a) shows the diffraction patterns taken from the tensile test specimen, from the beginning of loading to the final fracture. Phase transformation cannot be detected. Fig. 9(b) shows the variation of lattice strain with loading time for five different crystallographic planes, indicating a strong elastic anisotropy. It can be seen that {200} and {311} planes have the lowest elastic modulus, while {220} and {222} planes have the highest. For the Ni2.1 EHEA with the fcc/B2 composite structure, its deformation behavior is quite similar to that of traditional fcc alloys and other fcc-structured HEAs [26]. This scenario also echoes our previous argument for the decent but still limited ductility in the EHEA due to the role B2 phase plays. It is worth noting that {200} and {311} planes of the $AlCoCrFeNi_{2.1}$ EHEA can sustain larger lattice strain compared to the fcc-structured HEA reported previously [26], of above ~ 0.004 and ~ 0.003 till tensile fracture.

3.5 TEM analysis

TEM analysis was performed to further identify the structure of these eutectic and near-eutectic HEAs after tensile testing. The dark lamellar structure in Fig. 10 (a) is confirmed to correspond to the B2 phase, while the light lamellar structure corresponds to the ordered fcc ($L1_2$) phase, with their diffraction patters given in Fig. 10 (b-c). TEM results confirm that the Ni2.1 EHEA after tensile testing still comprise a mixture of (ordered) fcc and B2 phase, and there is no new phase formed during the tensile testing process, in agreement with the in-situ synchrotron XRD result. Fig.11 displays the microstructure of the Ni2.1 EHEA after tensile fracture. It is clear that a large number of dislocations occur in the soft fcc phase, while no dislocation are observed in the hard/brittle B2 phase. Dislocation slip was blocked in the fcc/B2 phase boundary. A higher dislocation density is seen in the fcc phase near the fcc/B2 phase boundary, compared to the dislocation density further inside the fcc phase. Except for dislocations, no detectable twinning was observed under TEM. It is therefore experimentally confirmed that the easy motion of dislocations in the soft fcc phase provides the N2.1 EHEA with high ductility, and the block-up of dislocations at the fcc/B2 phase boundaries provides the EHEA with high strength. Moreover, the long and straight dislocations and high density of dislocation debris demonstrate the strong interaction of multiple slip systems at room temperature. It is also noted that no deformation twins were observed under TEM.

4. Application potential of EHEAs in cryogenic environments

The simultaneous achievement of good castability and chemical homogeneity, and both high strength and high ductility at both room temperature and cryogenic temperatures, in directly cast industrial-scale EHEAs, provides these materials with great application potential in environments requiring directly cast materials (no subsequent thermomechanical treatment) with superior properties. Cryogenic environments, for example, can be the ideal occasion where EHEAs can find their applications. We use the propeller blades of the icebreaker as a specific example here to explain how directly-cast EHEAs can be the material of the choice in such an environment. An icebreaker is a special-purpose designed ship to move and navigate through ice-covered waters, and provide safe waterways for other ships. The external components of the icebreaker's propulsion system, including propellers and propeller shafts, determines its ability to propel itself onto the ice, break it, and clear the debris from its path successfully, are therefore essential for its safety. Mainly due to their irregular shape and large volume, propeller blades are prepared by direct casting and are not subject to subsequent thermomechanical treatments to further improve the mechanical performance. Thus, the directly cast materials need to satisfy the demanding application environments. The materials used for propeller blades of icebreakers must have high strength and high impact toughness (therefore high ductility) at low temperatures. Stainless steel and bronze are commonly used materials for propeller blades [27], but there remains a large room for these two materials to improve. Bronze have good castability and high ductility but its low strength is a concern, while stainless steels have poorer castability and their strength is also not high enough. The newly developed EHEAs, with excellent castability and chemical homogeneity and relatively low density (~ 7.4 g/cm^3 [21]) can therefore be the (much) better alternative materials for propeller blades. Our results (not shown here) also show that EHEAs containing high amount of Cr and Al, possess quite good corrosion resistance in the sea water, which is also a necessary material property as propeller blade materials.

5. Summary

To conclude, large-scale (~ 2.5 Kg) eutectic and near-eutectic $AlCoCrFeNi_x$ (x = 2.0, 2.1 and 2.2) HEAs with alternating fine $L1_2$/B2 lamellar structure were prepared, and their mechanical properties were evaluated at both room temperature and cryogenic temperatures. Tensile tests show that directly cast eutectic HEAs can exhibit both high strength and ductility in a comfortable compositional range, and also in a wide temperature range, which outperform most of conventional cast alloys and also HEAs reported previously. The deformation behavior and microstructure evolution of the eutectic and near-eutectic HEAs were carefully investigated by strain measurement using digital image correlation, in-situ synchrotron X-ray diffraction, and TEM. It is found that the strain field of the EHEA shows a wavy distribution and almost no necking occurs before fracture. The deformation behavior of EHEAs differs significantly from those of conventional fcc- and bcc-structured metals. The alternative soft fcc phase and hard B2 phase in the EHEA, which constitutes the fine lamellar microstructure, effectively delays the onset of necking. The good ductility of the EHEA is mainly provided by the dislocation motion in the soft fcc phase, while the pile-up of dislocations at the fcc/B2 phase boundaries provides the alloy with high strength, which however also limits the further deformation of the alloy. No detectable phase transitions occurred during deformation and no deformation twins were observed after the tensile testing. Our results further convince that EHEAs have great potential in industrial applications, particularly in cryogenic environments.

Acknowledgments

This research was supported by the National Science Foundation of China (Nos. 51525401, 51471044 and 51525401), the Fundamental Research Funds for Central Universities, Key Laboratory of Basic Research Projects, Department of Education of Liaoning Province (LZ2014007), and the Natural Science Foundation of Liaoning Province (2014028013). SG acknowledges the startup grant from Areas of Advance Materials Science at Chalmers University of Technology and the Junior Researcher Grant from the Swedish Research Council under grant 2015-04087. The research leading to these results has received funding from the People Programme (Marie Curie Actions) of the European Union's Seventh Framework Programme (FP7/2007-2013) under REA grant agreement no 608743.

References

[1] Gludovatz, B., Hohenwarter, A., Catoor, D., Chang, E. H., George, E. P., Ritchie, R. O., A fracture-resistant high-entropy alloy for cryogenic applications, Science, 345 (2014) 1153.

[2] Senkov, O. N., Miller, J. D., Miracle, D. B., Woodward, C., Accelerated exploration of multi-principal element alloys with solid solution phases, Nature Communications, 6 (2015).

[3] Santodonato, L. J., Zhang, Y., Feygenson, M., Parish, C. M., Gao, M. C., Weber, R. J. K., Neuefeind, J. C., Tang, Z., Liaw, P. K., Deviation from high-entropy configurations in the atomic distributions of a multi-principal-element alloy, Nature Communications, 6 (2015).

[4] Gludovatz, B., Hohenwarter, A., Thurston, K. V. S., Bei, H., Wu, Z., George, E. P., Ritchie, R. O., Exceptional damage-tolerance of a medium-entropy alloy CrCoNi at cryogenic temperatures, Nature Communications, 7 (2016).

[5] Zhang, Y., Stocks, G. M., Jin, K., Lu, C., Bei, H., Sales, B. C., Wang, L., Beland, L. K., Stoller, R. E., Samolyuk, G. D., Caro, M., Caro, A., Weber, W. J., Influence of chemical disorder on energy dissipation and defect evolution in concentrated solid solution alloys, Nature Communications, 6 (2015).

[6] Li, Z., Pradeep, K. G., Deng, Y., Raabe, D., Tasan, C. C., Metastable high-entropy dual-phase alloys overcome the strength-ductility trade-off, Nature, 534 (2016) 227.

[7] Zhang, Z., Mao, M. M., Wang, J., Gludovatz, B., Zhang, Z., Mao, S. X., George, E. P., Yu, Q., Ritchie, R. O., Nanoscale origins of the damage tolerance of the high-entropy alloy CrMnFeCoNi, Nature Communications, 6 (2015).

[8] Zou, Y., Ma, H., Spolenak, R., Ultrastrong ductile and stable high-entropy alloys at small scales, Nature Communications, 6 (2015).

[9] Kozelj, P., Vrtnik, S., Jelen, A., Jazbec, S., Jaglicic, Z., Maiti, S., Feuerbacher, M., Steurer, W., Dolinsek, J., Discovery of a superconducting high-entropy alloy, Physical

Review Letters, 113 (2014).

[10] Jiang, C., Uberuaga, B. P., Efficient Ab initio modeling of random multicomponent alloys, Physical Review Letters, 116 (2016).

[11] Yeh, J. W., Chen, S. K., Lin, S. J., Gan, J. Y., Chin, T. S., Shun, T. T., Tsau, C. H., Chang, S. Y., Nanostructured high-entropy alloys with multiple principal elements: Novel alloy design concepts and outcomes, Advanced Engineering Materials, 6 (2004) 299.

[12] Cantor, B., Chang, I. T. H., Knight, P., Vincent, A. J. B., Microstructural development in equiatomic multicomponent alloys, Materials Science and Engineering A, 375-377 (2004) 213.

[13] Zhang, Y., Zuo, T. T., Tang, Z., Gao, M. C., Dahmen, K. A., Liaw, P. K., Lu, Z. P., Microstructures and properties of high-entropy alloys, Progress in Materials Science, 61 (2014) 1.

[14] Lu, Z. P., Wang, H., Chen, M. W., Baker, I., Yeh, J. W., Liu, C. T., Nieh, T. G., An assessment on the future development of high-entropy alloys: Summary from a recent workshop, Intermetallics, 66 (2015) 67.

[15] Gao, M. C., Yeh, J.-W., Liaw, P. K., Zhang, Y. High-Entropy Alloys: Fundamentals and Applications. Cham, Switzerland: Springer, 2016.

[16] Wu, Z., Bei, H., Otto, F., Pharr, G. M., George, E. P., Recovery, recrystallization, grain growth and phase stability of a family of FCC-structured multi-component equiatomic solid solution alloys, Intermetallics, 46 (2014) 131.

[17] Gao, M. C., Alman, D. E., Searching for next single-phase high-entropy alloy compositions, Entropy, 15 (2013) 4504.

[18] Guo, S., Ng, C., Wang, Z. J., Liu, C. T., Solid solutioning in equiatomic alloys: Limit set by topological instability, Journal of Alloys and Compounds, 583 (2014) 410.

[19] Fu, Z., Chen, W., Wen, H., Zhang, D., Chen, Z., Zheng, B., Zhou, Y., Lavernia, E. J., Microstructure and strengthening mechanisms in an FCC structured single-phase nanocrystalline $Co_{25}Ni_{25}Fe_{25}Al_{7.5}Cu_{17.5}$ high-entropy alloy, Acta Materialia, 107 (2016) 59.

[20] Varalakshmi, S., Kamaraj, M., Murty, B. S., Synthesis and characterization of nanocrystalline AlFeTiCrZnCu high entropy solid solution by mechanical alloying, Journal of Alloys and Compounds, 460 (2008) 253.

[21] Lu, Y., Dong, Y., Guo, S., Jiang, L., Kang, H., Wang, T., Wen, B., Wang, Z., Jie, J., Cao, Z., Ruan, H., Li, T., A promising new class of high-temperature alloys: Eutectic high-entropy alloys, Scientific Reports, 4 (2014) 6200.

[22] Senkov, O. N., Wilks, G. B., Scott, J. M., Miracle, D. B., Mechanical properties of $Nb_{25}Mo_{25}Ta_{25}W_{25}$ and $V_{20}Nb_{20}Mo_{20}Ta_{20}W_{20}$ refractory high entropy alloys, Intermetallics, 19 (2011) 698.

[23] Gali, A., George, E. P., Tensile properties of high- and medium-entropy alloys, Intermetallics, 39 (2013) 74.

[24] Wani, I., Bhattacharjee, T., Sheikh, S., Lu, Y., Chatterjee, S., Bhattacharjee, P., Guo, S., Tsuji, N., Ultrafine-grained $AlCoCrFeNi_{2.1}$ eutectic high-entropy alloy, Materials Research Letters, DOI:10.1080/21663831.2016.1160451 (2016) 1.

[25] Otto, F., Dlouhý, A., Somsen, C., Bei, H., Eggeler, G., George, E. P., The influences of temperature and microstructure on the tensile properties of a CoCrFeMnNi high-entropy alloy, Acta Materialia, 61 (2013) 5743.

[26] Wu, Y., Liu, W. H., Wang, X. L., Ma, D., Stoica, A. D., Nieh, T. G., He, Z. B., Lu, Z. P., In-situ neutron diffraction study of deformation behavior of a multi-component high-

entropy alloy, Applied Physics Letters, 104 (2014) 051910.
[27] Carlton, J. Marine Propellers and Propulsion, 3rd Edition. Oxford, UK: Butterworth-Heinemann, 2012.

Table 1 Yield strength, fracture strength and elongation (EL%) to fracture of Ni2.0, Ni2.1 and Ni2.2 alloys at room temperature (RT), and -70 and -196 ºC

Test temperature	Alloys	σ_y (MPa)	σ_{UTS} (MPa)	EL%
RT	*Ni2.0*	545.6	1076	16.6
	Ni2.1	546.4	1046	17.7
	Ni2.2	544.5	1120	20.5
-70 ºC	*Ni2.0*	580	1034	10.5
	Ni2.1	595	1168	15.8
	Ni2.2	570	1143	18.0
-196 ºC	*Ni2.0*	715	952	3.7
	Ni2.1	690	1051	6.7
	Ni2.2	705	1151	9.3

Figure captions

Fig. 1 SEM image showing the microstructure of the bulk AlCoCrFeNix (x =2.0, 2.1 1, and 2.2) alloys: (a) hypoeutectic AlCoCrFeNi$_{2.0}$ alloy; (b) eutectic AlCoCrFeNi$_{2.1}$ alloy, and (c) hypereutectic AlCoCrFeNi$_{2.2}$ alloy.

Fig. 2 XRD pattern of AlCoCrFeNi$_x$ (x = 2.0, 2.1 and 2.2) alloys.

Fig. 3 Engineering tensile stress-strain curves of AlCoCrFeNi$_x$(x = 2.0, 2.1 and 2.2) alloys at RT.

Fig. 4 Engineering tensile stress-strain curves of the AlCoCrFeNi$_x$(x = 2.0, 2.1 and 2.2) alloy at -70 ^{o}C.

Fig. 5 Engineering tensile stress-strain curves of the AlCoCrFeNi$_x$ (x = 2.0, 2.1 and 2.22) alloy at -196 ^{o}C.

Fig. 6 Fracture surface morphology of the AlCoCrFeNi$_{2.1}$ EHEAs: (a) at -196 ^{o}C; (b) at -70 ^{o}C; (c) at RT.

Fig.7 Appearance of the tensile specimen at the end of the Nakazima test

Fig. 8 Nakazima test results measured at different time steps (stages) during tension: (a) the strain field of the AlCoCrFeNi$_{2.1}$ EHEA, presenting wave-like distribution; (b) and (c) the strain field of the pure Ni and pure Fe metal, showing the evolution of strain localization and necking development.

Fig. 9 (a) Selected X-ray diffraction patterns collected at different time steps during tensile loading at RT. (b) Loading time versus lattice strain curves for five crystal planes obtained during tensile loading at RT. The stresses at the 5th, 10th, 15th, 20th and 25th minute of the tensile testing process are extracted from the recorded stress as a function of loading time, and indicated on the plot.

Fig. 10 TEM images from the tensile Ni2.1 EHEA specimen stretched to fracture at RT: (a) Bright-field image showing the lamellar structure; (b) and (c) are the SADP (selected-area diffraction pattern) corresponding to the L1$_2$ and B2 phase, respectively. Superlattice diffraction spots are indicated by circles.

Fig. 11 TEM images from the tensile Ni2.1 EHEA specimen stretched to fracture at RT: (a) a large number of dislocations are observed in the L1$_2$ phase, but not in the B2 phase; (b) dislocations within the L1$_2$ phase.

Lu YP, et al., Fig. 1

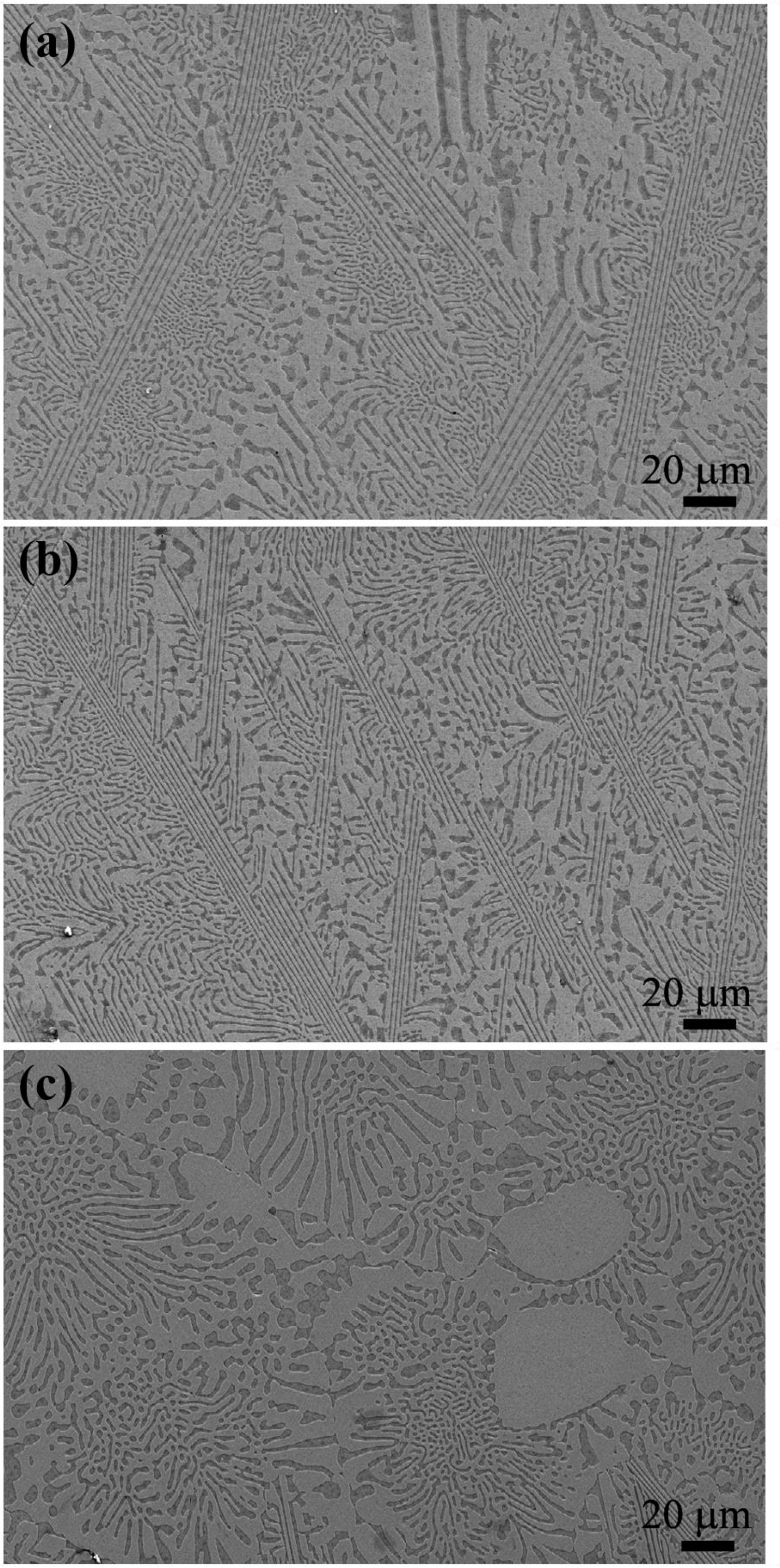
(a)
20 μm
(b)
20 μm
(c)
20 μm

Lu YP, et al., Fig. 2

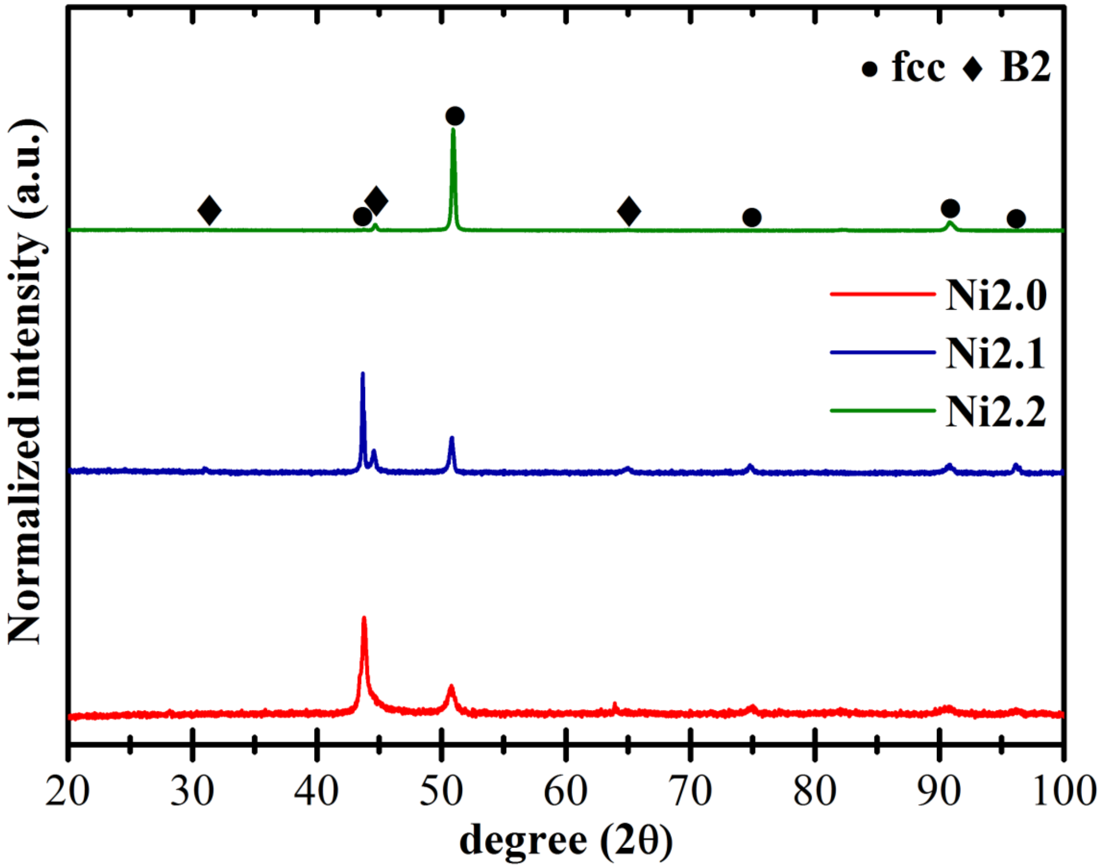

Lu YP, et al., Fig. 3

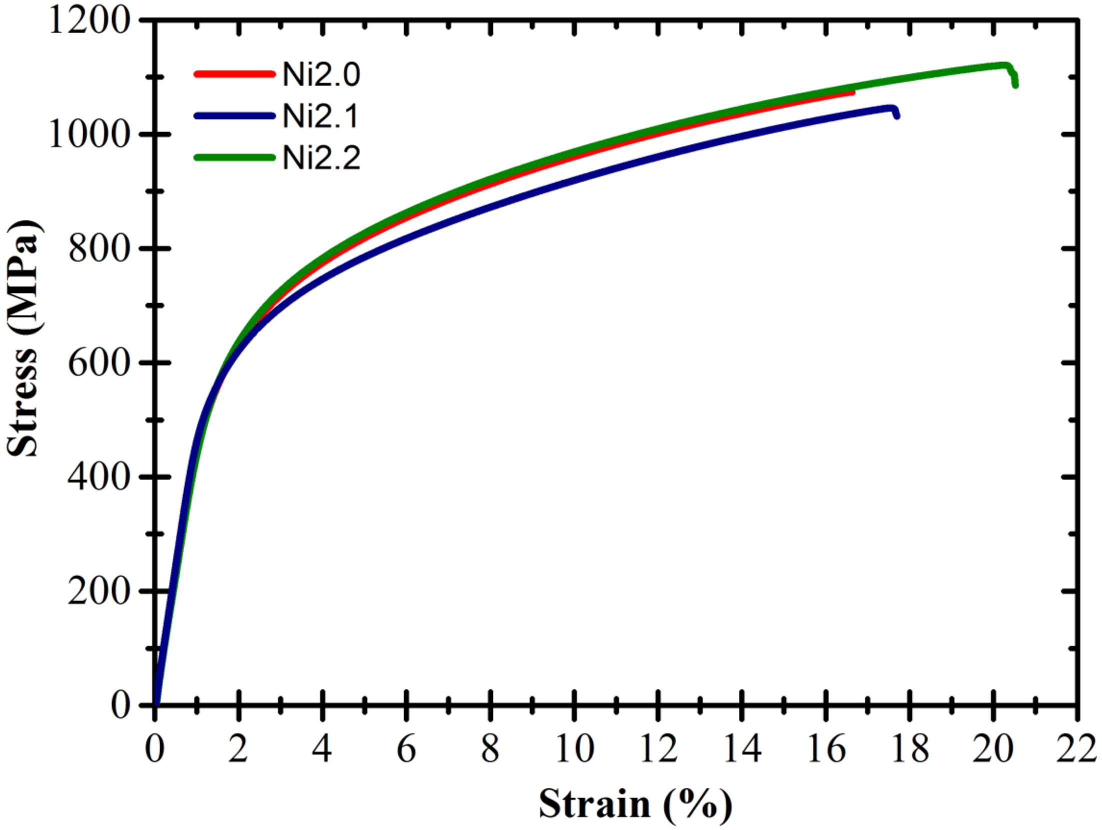

Lu YP, et al., Fig. 4

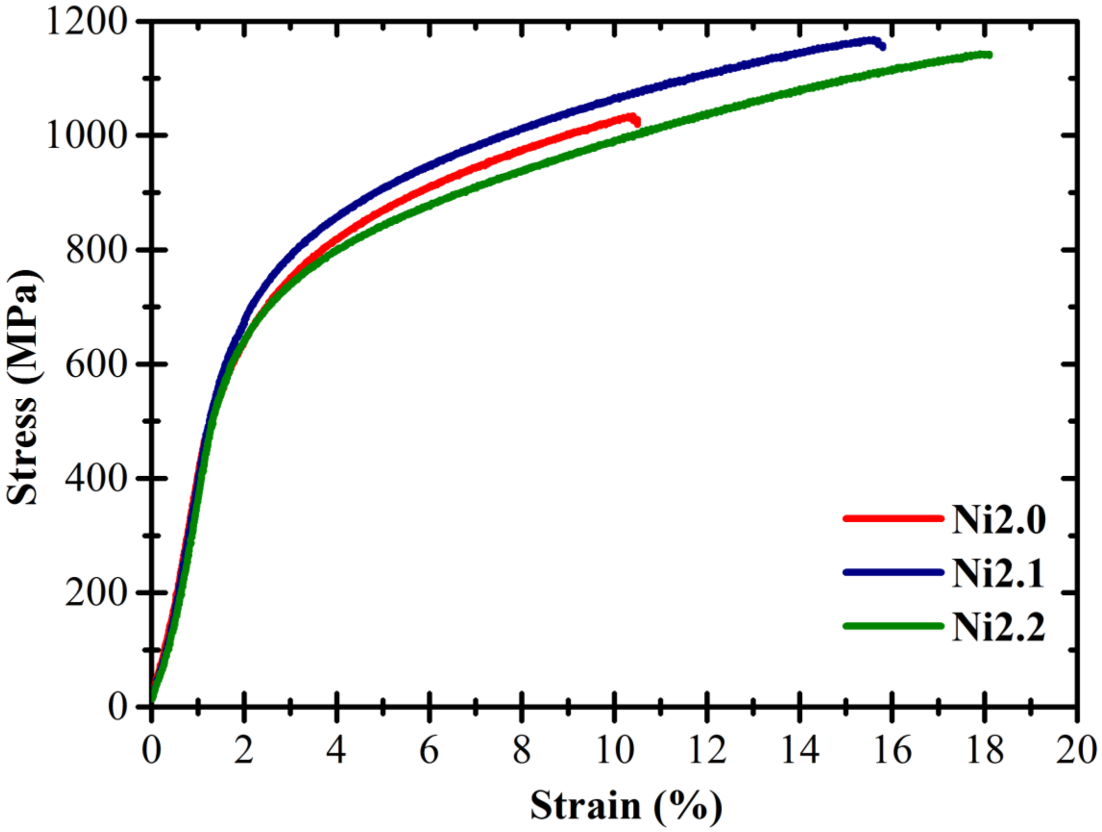

Lu YP, et al., Fig. 5

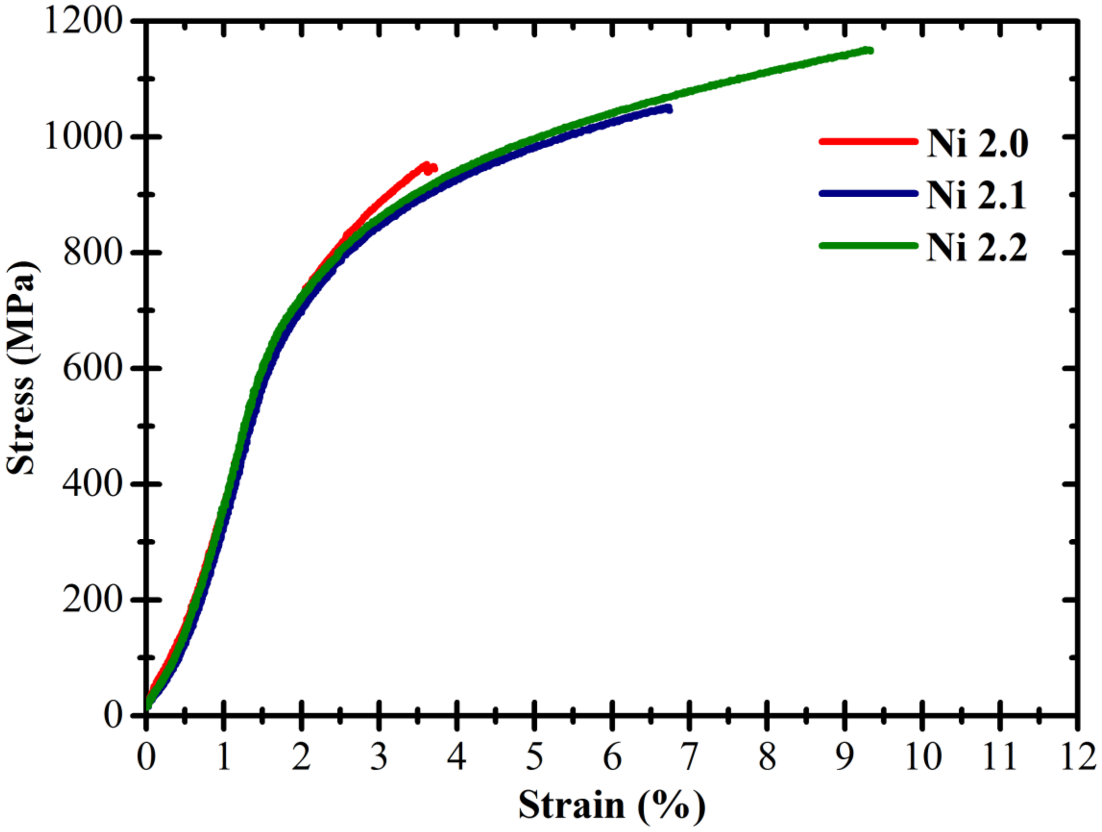

Lu YP, et al., Fig. 6

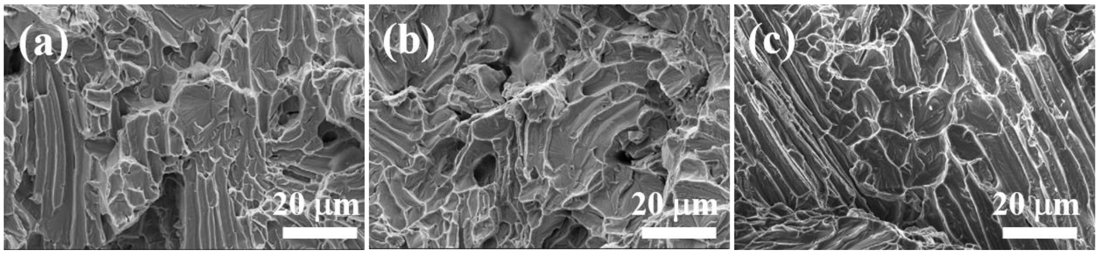
(a)
20 μm
(b)
20 μm
(c)
20 μm

Lu YP, et al., Fig. 7

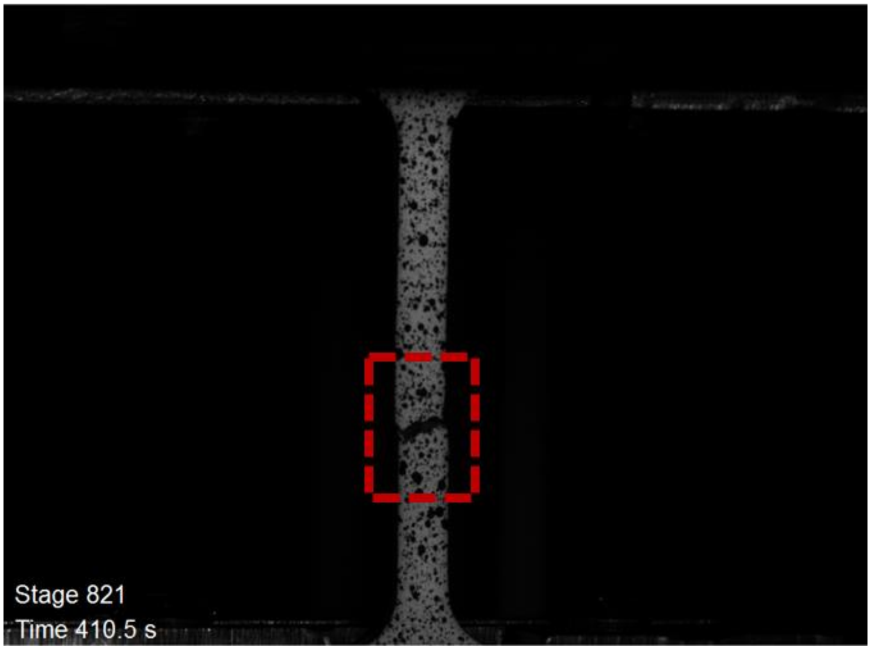
Stage 821
Time 410.5 s

Lu YP, et al., Fig. 8

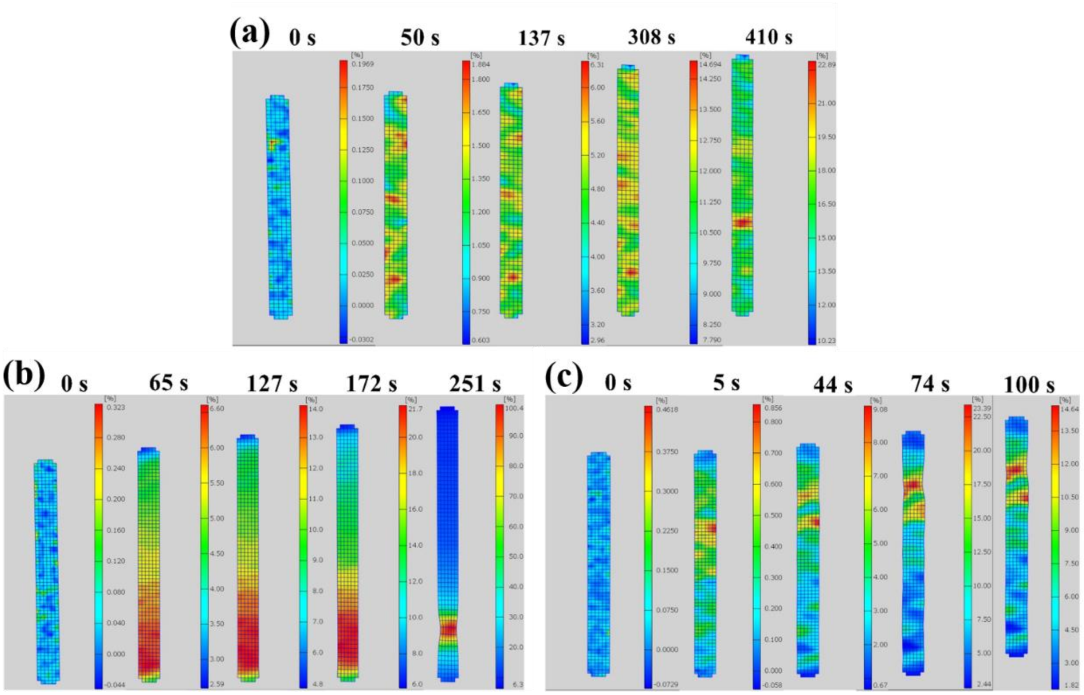

Lu YP, et al., Fig. 9

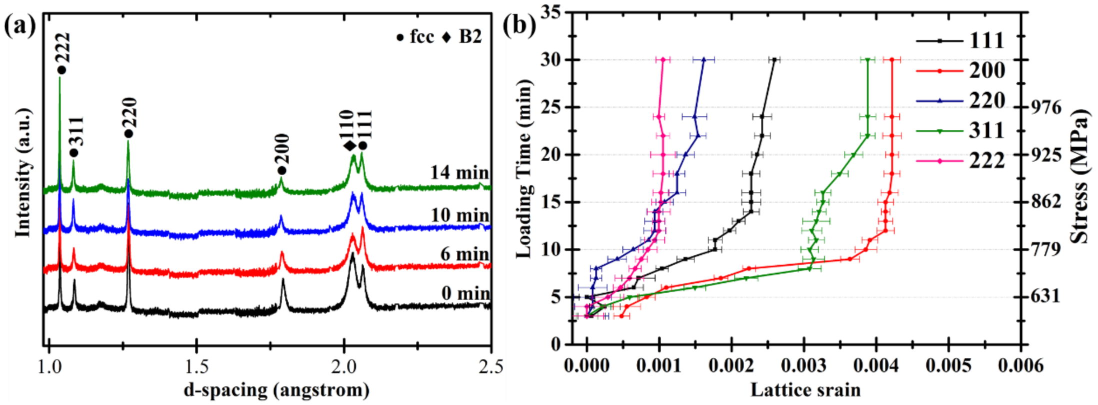

Lu YP, et al., Fig. 10

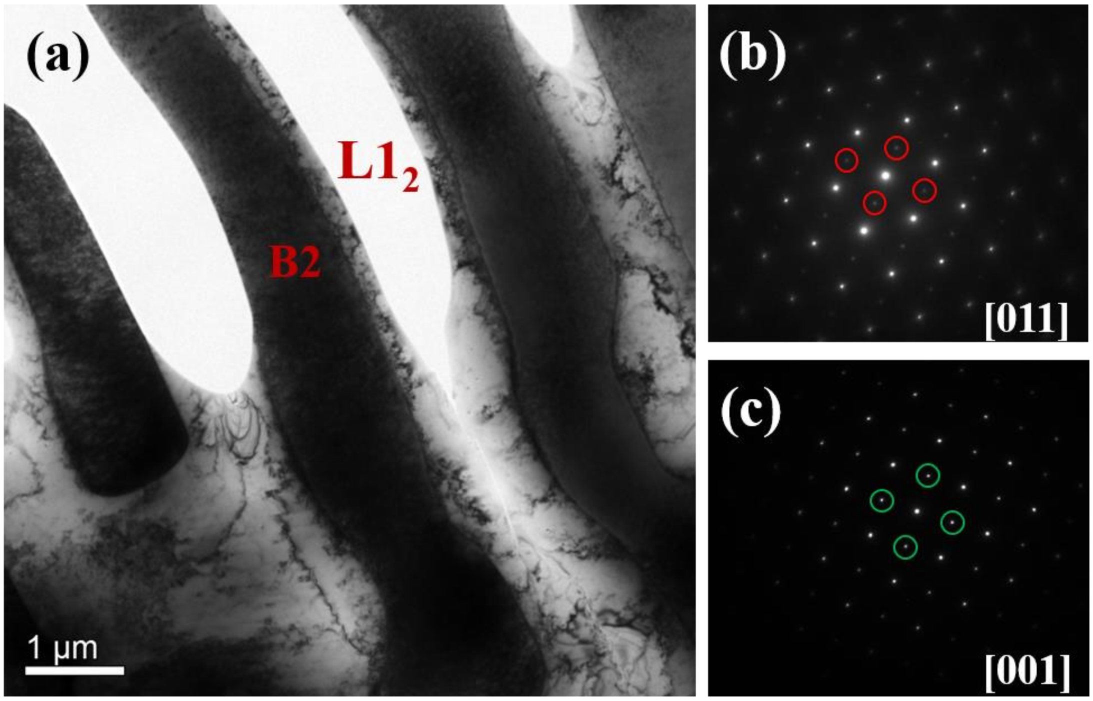
(a)
L1$_2$
B2
1 μm
(b)
[011]
(c)
[001]

Lu YP, et al., Fig. 11

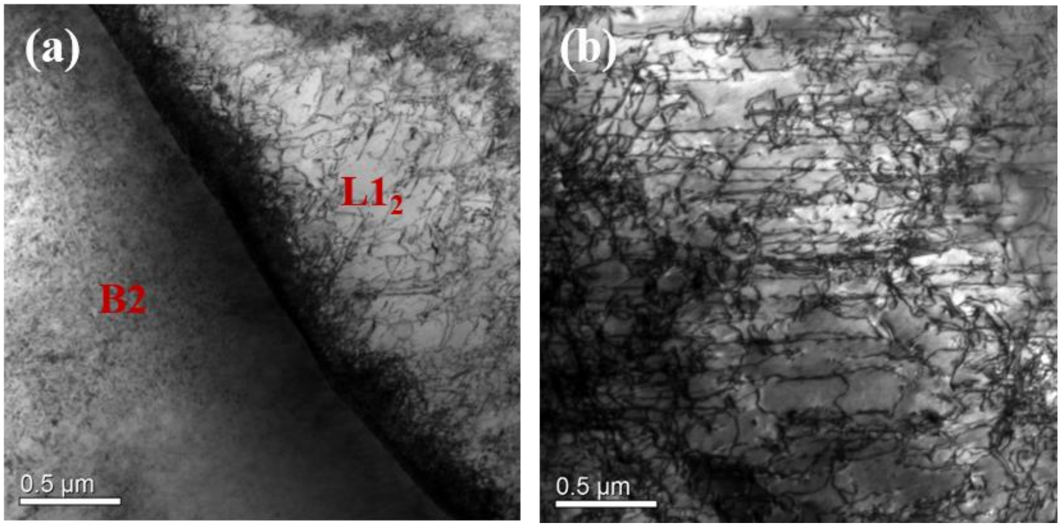
(a)
L1$_2$
B2
0.5 μm
(b)
0.5 μm